doi:10.20944/preprints202107.0675.v1

Article

Vertically Aligned Binder-Free TiO_2 Nanotube Arrays Doped with Fe, S and Fe-S for Li-ion Batteries

#Suriyakumar Dasarathan,[1,2] #Mukarram Ali,[2,3] Tai-Jong Jung,[2,3] Junghwan Sung,[1,2] Yoon-Cheol Ha,[3] Jun-Woo Park,[3] Doohun Kim[1,2]*

[1]Nano Hybrid Technology Research Center, Electrical Materials Research Division, Korea Electrotechnology Research Institute, Changwon 51543, Republic of Korea
[2]Department of Electro-Functionality Materials Engineering, University of Science and Technology (UST), Daejeon, Republic of Korea
[3]Next Generation Battery Research Center, Electrical Materials Research Division, Korea Electrotechnology Research Institute, Changwon 51543, Republic of Korea.

Corresponding Author

*Email: kdh0121@keri.re.kr
#S.D. and M.A. contributed equally to this work

ABSTRACT

Vertically aligned Fe, S, and Fe-S doped anatase TiO_2 nanotube arrays are prepared by electrochemical anodization process using an organic electrolyte in which lactic acid is added as an additive. In the electrolyte, nanotube layers of greater length (12 μm) and high order with inner diameter of approx. 90 nm and outer diameter of approx. 170 nm are achieved. Doping of Fe, S, and Fe-S via simple wet impregnation method substituted Ti and O sites with Fe and S, which leads to enhance the rate performance at high discharge current densities. Discharge capacities of TiO_2 tubes increased from 82 mAh g^{-1} (bare) to 165 mAh g^{-1} for Fe-S doped TiO_2 at high current densities of 0.3 $mAcm^{-2}$ after 100 cycles with exceptional capacity retention of 85% after 100 cycles. Owing to the enhancement of thermodynamic and kinetic properties by doping of Fe-S, Li-diffusion increased resulting in remarkable discharge capacities of 143 mAh g^{-1} and 89 mAh g^{-1} at a current density of 7.4 mA cm^{-2} and 19 mA cm^{-2}, respectively.

KEYWORDS: Li-ion batteries; Binder-free electrodes; TiO_2 nanotube arrays; Electrochemical anodization; Elemental doping

1. Introduction

Titanium based oxides have drawn great attention in the lithium ion battery world because better thermal stability than the conventional graphite anode[1]. Moreover, this class of active material shows other interesting features such as low cost, none-toxicity and small volume change process (2-3 %) during the lithium insertion and desertion, along with an excellent cycling life[1]. In general, bulk TiO_2 shows a low theoretical capacity of 175-360 mAh g^{-1} and a low electrical conductivity. The electrochemical performance and the reversible capacity of titanium based oxides mainly depend on their microscopic structure, morphology and particle size[2]. Interestingly, the nanostructured titanium oxide leads to a better capacity, longer cycling life and higher rate capacity than bulk TiO_2[2,3].

TiO_2 shows excellent safety and stability characteristics at the operation potential of 1.5 V vs Li/Li^+. Moreover, TiO_2 has high electro-activity, strong oxidation capability, good chemical stability, high abundance and structural diversity [4,6]. Where TiO_2 based materials possess boosting the performance of battery, still they face disadvantage such as poor electrical conductivity and low ion diffusion coefficients, which can lead to poor electrochemical performance thus hindering their commercial application[4,7]. So far many efforts have been developed to overcome this problem by means of using, for example, low-dimension (1 D, 2 D) TiO_2 nanostructures composites [8,9].

The reduction of $Ti^{4+}\rightarrow Ti^{3+}$ is accompanied by Li ion insertion/extraction into the oxide structure. Electrochemical fading in the crystal structure due to pulverizing of electrodes during volume expansion and reduction. In the advantage of taking forward TiO_2 nanotubes (TNTs) as anodes, i) the well-connected electrode geometry leads to the shortest ion diffusion path, ii) mechanical strain arising during Li ion insertion/desertion cycling can be much accommodated, and iii) therefore the structural stability is maintained[10].

On the other hand, doping the heteroatoms including C, Nb, N, B, W, Sn, and Fe into TiO_2 nanostructures is a promising way to stabilize these structures and improve the electron flow to accelerate the kinetics during electrochemical processes[11-15]. This will directly improve the rate performance, cycling behavior, and specific capacity of TNTs in Li-ion battery application. However, the extremely low thermodynamic solubility of the dopants in TiO_2 faces many challenging obstacles once the dopant locates at interstitial sites[16]. Therefore, a co-doping idea has been presented to overcome the limitation. So the concept of co-doping (including carbon, nitrogen; fluorine, nitrogen; chromium, nitrogen; and sulfur, nitrogen) has been applied in TiO_2 nanoparticles as an anode material for Li-ion battery [2,8,9,12,15,17-19] . In the previous studies, it has been demonstrated that the Fe-S co-dopant pairs can substantially narrow band gap and effectively modify the electronic structure of TiO_2[9,19]. However, there have not been many studies on doping of TNTs for the Li-ion battery anode[1,18].

In this study, vertically aligned self-organized TiO_2 nanotubes are prepared by electrochemical anodizing technique[22,23]. Fe-S co-doping was performed using a wet impregnation method. Owing to the improved electrical conductivity and lithium ion diffusion coefficient, Fe-S co-doped TNTs shows an improved electrochemical performance including excellent cycling stabilities and remarkable rate performances, without slurry casting so called binder free electrodes.

2. Materials and Methods

2.1. Preparation of TNTs

Pre-cleaned Ti-foils (0.1 mm thick, 99.99 % purity, Nilaco) were electrochemically anodized in an electrolyte composed of 1.5 M lactic acid, 0.1 M ammonium fluoride and 5 wt. %

deionized water in ethylene glycol[24]. The anodization was carried out in a two electrode cell configuration: a Pt mesh was used as the counter electrode and the Ti foils were used as the working electrode. The anodization was conducted by using a high-voltage potentiostat (OPS-22101, ODA, Korea) at a DC voltage of 120 V for 300 s, 600 s, and 800 s with the electrolyte temperature at 60 ºC as shown in figure 1. The obtained samples were rinsed in ethanol and dried in an oven at room temperature.

2.2. Preparation of Fe-S co-doped TNTs

Fe, S, and Fe-S co-doped samples were prepared by using simple wet impregnation method as mentioned in a previous report [19]. The anodized samples were immersed in $FeCl_3·6H_2O$, in thio- urea, and in a mixture of $FeCl_3·6H_2O$ and thio-urea, each dissolved 20 ml of ethanol solution for one hour and kept in an oven for room temperature drying in air atmosphere to produce Fe, S, and Fe-S doped TNTs, respectively. In order to obtain the crystalline anatase phase in TNTs the dried samples were annealed at 500 ºC for 3 hrs under air by using a tube furnace (XY-1400S, Hantech, Korea) as shown in figure 1.

2.3. Materials characterization

The morphological study of the synthesized materials was performed using a field-emission microscope (Hitachi FE-SEM S4800) equipped with energy dispersive spectroscopy as well. The structure and crystalline phase of the samples were characterized by X-ray powder diffraction (XRD, Philips, X-pert PRO MPD) with Cu Kα ($\lambda = 0.15406$ nm). The electronic states of elements were characterized by X-ray photoelectron spectroscopy (XPS, K-Alpha + XPS System, Thermo Scientific UK). XPS was conducted with a monochromatic Al Kα source ($h\upsilon$ = 1486.6 eV) with a spot size of 400 µm.

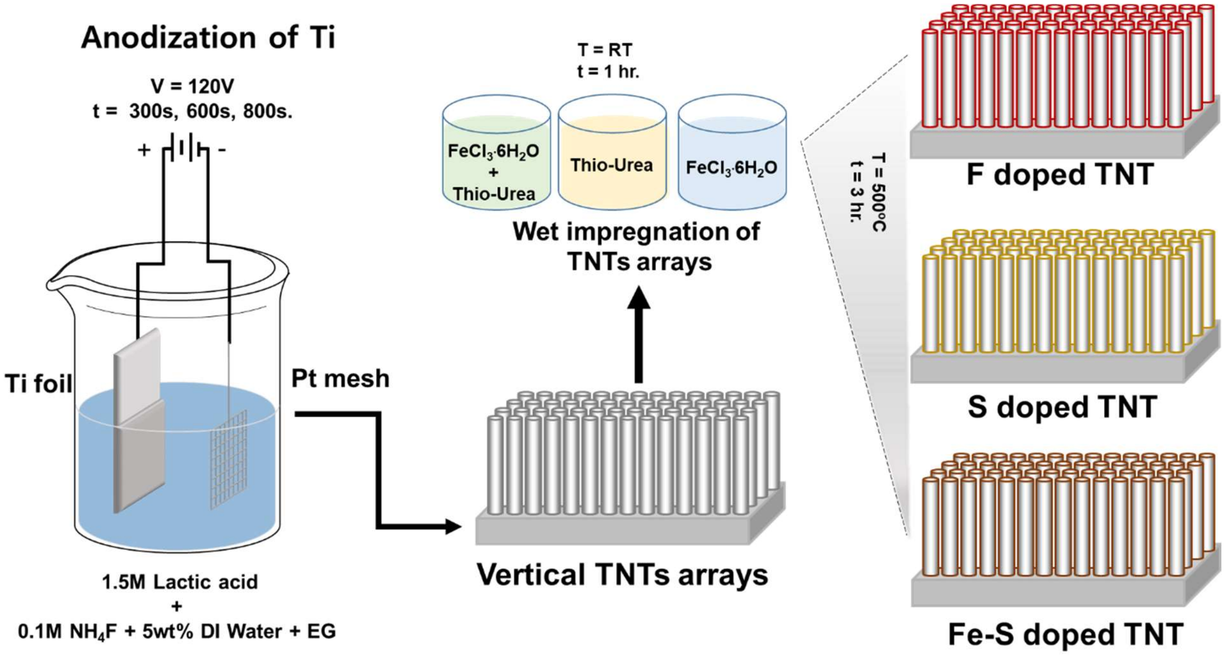

Figure 1. A schematic illustration of the preparation steps for Fe, S, and Fe-S doped TNTs.

2.4. Electrochemical characterization

The vertically aligned TNTs arrays doped with Fe, S, and Fe-S grown on Ti foils was cut into disk (diameter of 14 mm) and used as the anode for the electrochemical tests. A coin half-cell with a polypropylene membrane separator (Celgard 2325, Celgard Inc., USA) and a Li-metal foil (thickness = 500 μm, purity 99.9%) as the counter-electrode was used to evaluate the electrochemical performance. The TNT disks were directly fabricated as a (the working electrode) in the electrochemical cell without adding any conductive carbon or binder. The electrolyte was 1 M $LiPF_6$ dissolved in 1:1:1, v/v/v mixture of ethylene carbonate, dimethyl carbonate, and ethyl methyl carbonate (EC: DMC: EMC) with 5% FEC. The assembled cells were galvanostatically cycled at current densities ranging from 0.1 mA cm^{-2} to 19 mA cm^{-2} in a potential range of 0.5–3 V using a multi-channel battery tester (MACCOR).

Cyclic voltammetry (CV) was performed by using an electrochemical workstation (VMP3, Bio-Logic, France) with the same coin cell in the scan range of 0.5–3.0 V at a scan rate of either 1 mV s^{-1} or 0.5 mV s^{-1}. Electrochemical impedance spectroscopy (EIS) test was performed by using an electrochemical workstation (VSP-300, Bio-Logic, France) in the frequency range of $10^{-2} – 10^{+5}$ Hz.

3. Results and discussion

3.1. Morphology and crystal structure

Self-organized vertically aligned (TNTs) were prepared via electrochemical anodization of Ti foils in the lactic acid added F^- ion containing electrolyte with 120 V at 60 ºC for 300 s, 600 s, and 800 s to obtain layer thickness of 12 μm, 36 μm, and 60 μm, respectively. The length of the nanotubes mainly depends on the anodizing time, applied voltage, electrolyte temperature, etc [25]. Lactic acid added electrolyte was used to obtain a high layer thickness (i.e. a long length) in relatively short time [24]. Figure 2a, 2b, and 2c shows the FE-SEM results for the prepared TNTs with different anodizing time. The inset figure 2a(i) shows the top view image which represents highly ordered TNT array having a uniform porosity, while figure 2a(ii) shows a cross-sectional view image which indicates the vertically aligned TNT array, and figure 2a(iii) shows the bottom view image of the hexagonally close packed TNT structure [23].

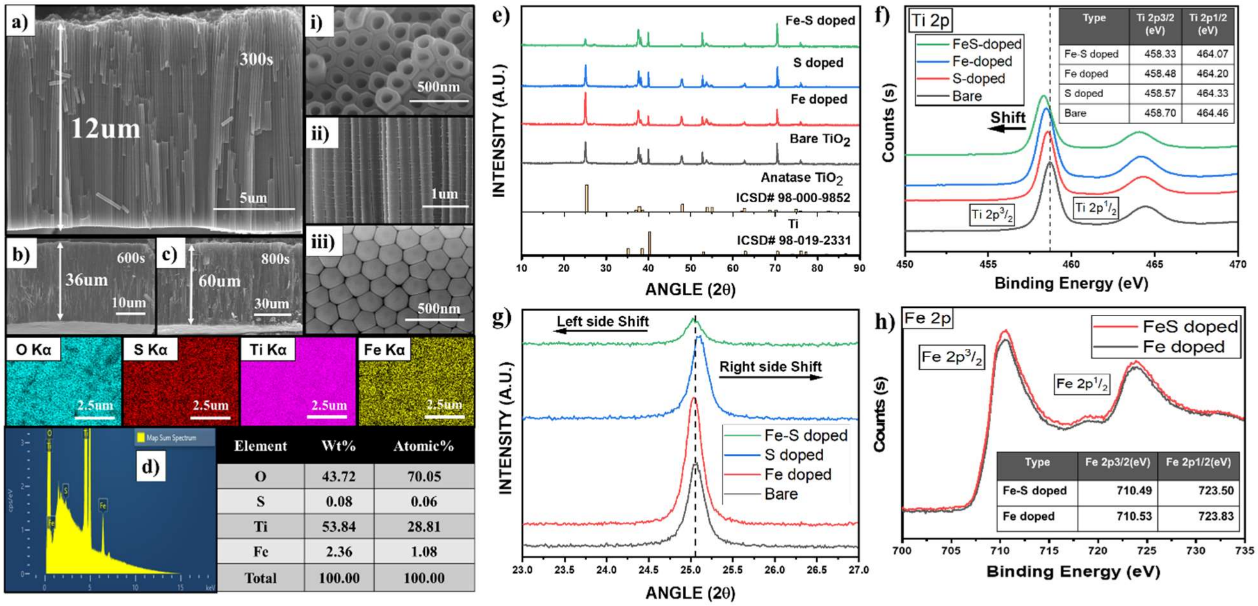

Element	Wt%	Atomic%
O	43.72	70.05
S	0.08	0.06
Ti	53.84	28.81
Fe	2.36	1.08
Total	100.00	100.00

Type	Ti 2p3/2 (eV)	Ti 2p1/2 (eV)
Fe-S doped	458.33	464.07
Fe doped	458.48	464.20
S doped	458.57	464.33
Bare	458.70	464.46

Type	Fe 2p3/2(eV)	Fe 2p1/2(eV)
Fe-S doped	710.49	723.50
Fe doped	710.53	723.83

Figure 2. (a), (b), and (c) shows FE-SEM images of as prepared TNTs. 12 µm, 35 µm, and 60 µm TNTs were successfully prepared by anodization process. a(i), a(ii), and a(iii) shows top, cross-section, and bottom view of 12 µm TNTs. **(**d) EDS result for Fe-S doped TNTs prepared

doi:10.20944/preprints202107.0675.v1

by the immersion technique. (e) XRD results for bare, Fe doped, S doped, and Fe-S doped TNTs. (f) Ti 2p XPS results for bare, Fe, S, and Fe-S doped TNTs showing a peak shift towards lower energies due to the presence of doped elements in the TNTs framework. (g) A zoomed in view of (011) XRD peak Showing clear peaks shifts for Fe, S, and Fe-S doped TNTs. (h) Fe 2p XPS results for Fe and Fe-S doped TNTs showing the incorporation of Fe in the TiO_2 framework.

Fe, S, and Fe-S co-doped TNTs are prepared by the approach shown in figure 1. Figure 2d shows the EDS mapping result for Fe-S doped TNTs and clearly shows the even distribution of the doped elements. Figure 2e shows the XRD patterns for bare, S, Fe, and Fe-S doped TNTs. It reveals the existence of the anatase TiO_2 for all the doped samples after annealing at 500 °C for 3hrs with characteristic peaks at 12.65° and 24.025° (ICSD# 98-000-9852). A high peak intensity of the (004) orientation can be observed in all of the TNTs, which indicates a high percentage of (011) orientation in the growth direction of the TNTs (figure S1a†). Moreover, doping of different atoms did not affect the orientation except the intensity difference in (011) peak[19]. In figure 2g, the diffraction peaks (011) of Fe doped TNTs and Fe-S doped TNTs shift to lower angles and the lattice parameters d_{011} are increased slightly from 0.350 nm for bare to 0.454 nm and 0.455 nm for Fe and Fe-S doped TNTs, respectively. This occurs due to the incorporation of Fe^{3+} (0.650 Å) having larger radius than Ti^{4+} (0.606 Å), suggesting that the Fe atoms have been successfully incorporated into the crystal structure of TiO_2[12,19]. However, in case of S doped TNTs, the peak shift is towards a higher angle. This phenomenon can be attributed towards the larger radius of Ti^{4+} (0.606 Å) than S^{4+} (0.370 Å) and S^{6+} (0.290 Å) [26]. However, the doping amount of S is kept very small in both Fe-S and S doped TNTs due to its high reactivity. Hence the effect is minimal in the lattice parameter change (Table S1†). Similarly, the effect of the doping on crystallite size can also be observed. The crystallite size decreases significantly as a result of S and Fe-S doping, while in case of Fe doping the decrease in the crystallite size is not as drastic as the former ones. The average crystallite size, calculated from Scherrer equation of Fe-S doped, Fe doped, S doped, and bare TNTs are approximately 32.38 nm, 39.636 nm, 30.319 nm, and 45.93 nm, respectively (Table S1†).

The electronic states of the dopants and the parent atoms in TNTs were analyzed by (XPS). As illustrated in figure 2f, the most intense peaks at 458.70 eV and 464.46 eV correspond to Ti 2p3/2 and Ti 2p1/2 spin–orbit splitting peaks, respectively. This suggests that Ti^{4+} is the predominant state of the Ti in bare TNTs. In the case of Fe doped TNTs, S doped TNTs, and Fe-S doped TNTs the peaks shift towards lower energy. This confirms the presence of dopants which have replaced Ti and O atoms due to the difference in the ionization energy decreases[27,28]. In case of Fe-S doped TNTs, not only S^{+2} and S^{+6} replaced Ti but there is a small peak observed at 163.01 eV (figure S1c†) which shows that there is also S^{-2} replacing O^{-2} as well [29].

Figure 2h shows the XPS spectrum of Fe 2p, where the binding energies at 710.53 eV, 723.83 eV, and 710.49 eV, 723.50 eV corresponding to Fe 2p3/2 and Fe 2p1/2 can be easily observed in Fe doped and Fe-S doped samples. This indicates that the doped Fe is mainly in 3^+ oxidation state. Due to the similarities of the radius between Fe^{3+} (0.650 Å) and Ti^{4+} (0.606 Å), Fe^{3+} can be incorporated into the lattice of TiO_2 to form Ti–O–Fe bonds [12]. In the case of S and Fe-S doped TNTs, the doping amounts for S are extremely small as discussed previously and accordingly S2p spectra is not observed in case of S however, in case of Fe-S doped TNTs S peaks were observed. In figure S1b†, the O 1s XPS spectra of Fe-S doped TNTs are split as two peaks. The energy of the peak located at 529.56 eV is equal to the O 1s electron binding energy for TiO_2. The other peak at 531.13 eV is ascribed to S–O–S bond, which confirms that the sulfur atoms replace a part of Ti sites [30] and in figure S1c† peak located at 163.01 eV [29]. This shows that sulfur is present in the form of S^{2-} by replacing O^{2-} which contradicts the previous report using thio-urea as a dopant precursor for sulfur[31]. According to the results of the XPS spectra, the atomic ratios of Fe, S, Ti, and O in Fe-S doped TNTs are approximately 3.01%, 0.1%, 24.68%, and 72.21%, respectively. This remarkable structural stability is expected to be conducive to reversible lithium storage with excellent cycle performances.

3.2. Electrochemical performance

In order to investigate the effect of different dopants in TNTs on the electrochemical performances, cyclic voltammetry experiments for bare and doped TNTs electrodes were conducted at 0.5 mV s^{-1} (figure 3a). The higher scan rate was chosen in order to mimic the effect of fast charging/discharging. Moreover, CV for TNTs with different thickness were also done 1 mV s^{-1} to investigate the effect of higher thickness on lithiation/delithiation of TNTs (figure 3b). In principle, the reaction equation can be used to express the lithium insertion and extraction in anatase TNTs electrode:

$$TiO_2 + nLi^+ + ne^- \leftrightarrow Li_nTiO_2 \qquad (1)$$

All the sample electrodes (figure 3a) exhibit peak couples at 2.14 / 1.63 V (bare TNTs), 2.17 / 1.67 V (S doped TNTs), 2.19 / 1.64 V (Fe doped TNTs), and 2.20 / 1.66 V (Fe-S doped TNTs) corresponding to the transition of Li poor α-Li_xTiO_2 ($0.01< x \leq 0.21$) with anatase structure to the orthorhombic β Li_xTiO_2($x\sim0.55$) phase , their positions are in good agreement with those reported in the literature [33-35]. In case Fe-doped TiO_2 in reduction peaks, there is an additional reaction happens due to the over potential of phase transformation from TiO_2 to Li_xTiO_2. In order to reduce the polarization effect happens between the electrode and electrolyte interface, the Fe-doping in TiO_2 will reduce this effect and enhance the electronic conductivity, which results that further charge/discharge reversibility is enhanced [43]. Moreover, there is a small peak pair visible at 1.62 V (lithiation) and 1.4 V (delithiation), which corresponds to a second phase change to fully lithiated $LiTiO_2$[33]. This feature is more prominent in the case of higher-length tubes as shown in figure 3b. Moreover, it can be seen that upon delithiation peak broadening is observed which is a characteristic for self-oriented TNTs[35]. In contrast to bare, S doped, and Fe doped TNTs, Fe-S doped TNTs show a prominent second phase transition upon delithiation.

The diffusion coefficient of lithium ion during the Li^+ intercalation/de-intercalation processes can be calculated according to Randles–Sevcik equation [36]. Figure 3d and S4b† shows the calculated diffusion coefficient values for doped TNTs and elongated TNTs. The Li^+ diffusion increases by doping of S, Fe, Fe-S. In case of doping Li^+ ion diffusion increased from 0.75×10^{-11} $cm^2\,s^{-1}$(bare TNTs) to 0.13×10^{-10} $cm^2\,s^{-1}$ (Fe-S doped TNTs) for de-intercalation and 0.2×10^{-11} $cm^2\,s^{-1}$ (bare TNTs) to 0.12×10^{-10} $cm^2\,s^{-1}$ (Fe-S doped TNTs) for intercalation. It should be noted that Li^+ diffusion is greatly improved by co-doping with both Fe and S in anodic TNT's framework.

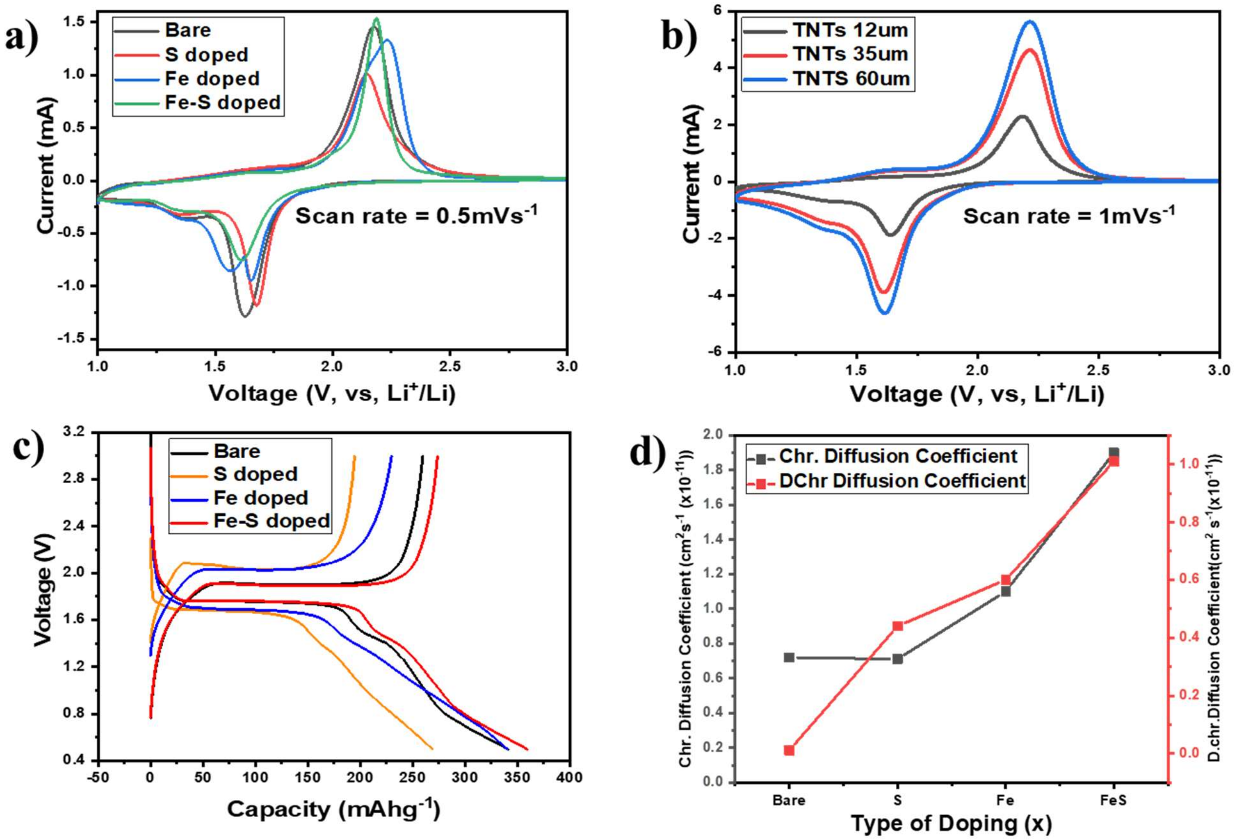

Figure 3. (a) Cyclic voltammograms of bare, Fe doped, S doped, and Fe-S doped TNTs with respect to Li metal at a scan rate of 0.5 mV s^{-1} **(b)** Cyclic voltammograms of TNTs with the different thickness of 12 μm, 36 μm, and 60 μm. **(c)** 1st charge-discharge profiles of bare, Fe, S, and Fe-S doped TNTs at current density of 0.3 mA cm^{-2} **(d)** Diffusion coefficient values calculated from Randles–Sevcik equation for bare, Fe, S, and Fe-S doped TNTs.

Moreover, preferentially oriented tubes are derived by anodization process and even directly use of these TNTs in LIB increases the charge/discharge capacities[35,37,38]. However these performances are considerably enhanced by co-doping with Fe-S in the TNT structures. In addition, the CV curves at a scan rate of 0.5 mV s^{-1} as shown in figure S2† are stable with almost overlaps from the second cycle, which indicate well posited dopant in the structures and excellent stability for Fe, S, and Fe-S doped TNTs electrodes.

Galvanostatic charging/discharging was carried out at current density of 0.3 mA cm^{-2} (0.2 C) in the range of 0.5-3.0 V vs. Li^{+}/Li^{-}, Initial discharge capacities for bare, S doped, Fe doped, and Fe-S doped TNTs anodes came out to be around 339 mAh g^{-1}, 268 mAh g^{-1}, 341 mAh g^{-1}, and 360 mAh g^{-1} (figure 3c). It can be seen that the discharge capacities for S doped TNTs is lower as compared to others, this is because of the reaction of sulfur with Li to form Li$_x$S which in result decreases the discharge capacity [39]. However, further in this study it will be shown that this does not affect the cycling behavior of TNTs but increase cyclability of S doped TNTs. It can also be observed that the charge (1.9 V) and discharge (1.65 V) plateaus for Fe-S doped TNTs show lowest and highest among the other electrodes, respectively. This indicates the lowest electrochemical polarization and the best charge/discharge energy density of Fe and S doped TNTs anode. Moreover, the specific capacity is proportional to time interval (i.e. scan rate) of charge/discharge [11,39] . The sloping region for the Fe-S doped TNTs electrode below the plateau corresponds to the pseudo-capacitive lithium storage in the surface area [40].

$$C=i/(dV/dT) \qquad (2)$$

Hence the sloping region will indicate the pseudo-capacitive lithium storage in the structures of TNTs. This shows that the shallowest slope (dV/dc) observed with the Fe-S doped TNTs electrode represents the highest capacitance values as compared to the steep slopes from the other three kinds of electrodes, thus increasing the capacity of TNTs form 339 mAh g^{-1} for bare TNTs to 360 mAh g^{-1} for Fe-S doped TNTs.

In figure S3, both areal and gravimetric capacities are shown for bare and Fe-S doped TNTs. It is clear that Fe-S doped TNTs show better cycling as compared to bare TNTs. Moreover, in case of Fe, S, and Fe-S after 60 cycles (figure 4a), they show higher discharge capacities of 118 mAh g^{-1}, 157 mAh g^{-1}, and 175 mAh g^{-1} as compared to 89 mAh g^{-1} of bare TNTs. Fe-S and bare doped TNTs were further cycled to 100. In the cycling results, it was found that Fe-S retained 85% discharge capacity (taken after 3rd cycle) as compared to bare TNTs with 65% (i.e. doping of Fe and S together increases the capacity retention and increased capacitive properties). Moreover, columbic efficiency in the 1st cycle is 76% for Fe-S doped TNTs and 72% for bare TNTs. These high irreversible capacities can be because of the higher length of the tubes and side reactions with sulfur and absorbed moisture due to high specific surface area[41]. However, this is redeemed in the 2nd cycle with 90.9% for Fe-S and 93.8% for bare TNTs. The decrease in columbic efficiency for Fe-S as compared to bare TNTs can be because of reaction of Li with S to form Li_xS , however, this product is redox active[39]. Hence this will help in further cycling and increase the electrochemical stability with the high capacity retention as shown in figure 4a.

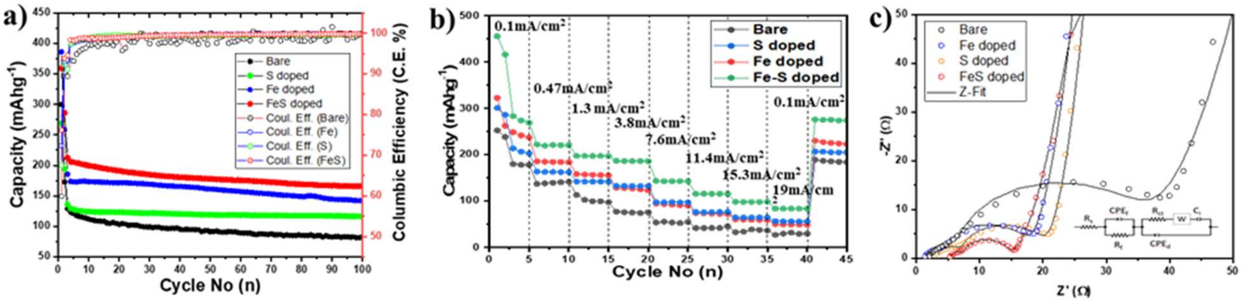

Figure 4. (a) Cycle vs discharge capacity curves for bare, Fe doped, S doped, and Fe-S doped TNTs cycled at 0.3 mA cm^{-2} current density. **(b)** Rate capablity of bare Fe doped, S doped, and Fe-S doped TNTs **(c)** EIS curves for bare, Fe doped, S doped, and Fe-S doped TNTs after 100 cycles.

Figure 4b shows rate capability cycling results for bare, Fe doped, S doped, and Fe-S doped TNTs. It is evident that Fe-S doped TNTs shows the best rate capabilities at very high current densities form 0.1 mA cm^{-2} to 19 mA cm^{-2}. All the doped TNTs showed exceptional rate capabilities at higher rates as compared to bare TNTs. Fe-S doped TNTs show 143 mAh g^{-1} at 7.4 mA cm^{-2} and 89 mAh g^{-1} at 19 mA cm^{-2} current densities as compared to 54 mAh g^{-1} at 7.4 mA cm^{-2} and 30 mAh g^{-1} at 19 mA cm^{-2} current densities for bare TNTs. It is important to note that Fe-S doped TNTs retained the reversible specific capacities of 275 mAh g^{-1} at 0.1 mA cm^{-2} as well when cycled again. These results clearly validate that the Fe-S doped TNTs electrodes exhibit superior lithium storage properties with prolonged cycle life and great rate capability for the fast discharge process.

To further understand the origin of the superior electrochemical properties of doped TNTs and to study differentiate kinetic and thermodynamic properties of the TNTs electrodes upon lithiation and delithiation, electrochemical impedance spectroscopy (EIS) was employed in the frequency range of 10^{-2} – 10^{+5} Hz. This allows for differentiation of processes taking place at different time scales during Li insertion and extraction. Figure 4c shows us the EIS spectrum and the fitting circuit of bare, S doped, Fe doped, and Fe-S doped TNTs after 100 cycles. In all of the observed EIS spectrums, at the highest frequencies, a depressed semicircle can be observed, which corresponds to the parallel combination of surface film resistance R_f and surface film capacitance C_f [35,40]. These thin surface films originate from the decomposition of compounds from the carbonate-based (EC, DMC) $LiPF_6$ electrolytes [42]. The second medium-frequency semi-circle relates to the interfacial charge transfer, represented by the charge transfer resistance, R_{ct}, and the double-layer capacitance, C_{dl}, in parallel. This is the most important parameter as R_{ct} determines the charge transfer during lithiation/delithiation. At lower frequencies, capacitive behavior is dominant, which can be observed by a steep line with an angle higher than 45° in the pointing out the initial part of a capacitive element [7]. It can be seen that, after 100 cycles R_{ct} values decreased when compared to bare TNTs electrode. R_{ct} values of 20.78 ohm, 18.49 ohm, and 15.54 ohm were achieved for S doped, Fe doped, and Fe-S doped TNTs as compared to 38.47 ohm for bare TNTs. However, in the nanotube system, the charge transfer may not be the only rate-determining step; therefore, it is also necessary to consider solid state diffusion in the bulk material [34]. This shows that both the increase in Li^+ diffusion and charge transfer resistances of doped TNTs increased the cycling and rate cycling properties. In order to observe the difference between before and after cycling effect in Fe-S doped TNTs, EIS was done before cycling of Fe-S doped TNTs samples as well. Figure S4a† shows the EIS spectrum and fitting of before and after 100 cycles. It can be observed that R_{ct} values for Fe-S doped TNTs decreased from 269 ohm to 15.54 ohm after 100 cycles. During lithiation, in case of TiO_2, fully lithiated Li_1TiO_2 forms with higher charge resistance, moreover, the decomposition of $LiPF_6$ electrolyte to LiF and Li_2CO_3 also increase the charge transfer resistance between electrode/electrolyte interfaces. However, by the introduction of Fe and S as co dopants the fully lithiated phase transition is suppressed which decreases the charge transfer resistance and as a result higher reversibility during lithiation and de-lithiation is achieved [35].

This incredible increase in electronic conductivity and charge transfer can be attributed towards the modified electronic structure resulting in exceptional properties and uniform pathways for Li^+ intercalation/de-intercalation. Electrochemical anodization to prepare TNTs improved the structural as well as the directional properties of as prepared TNTs. Primary nanocrystals of TiO_2 which were smaller in size shortened the electronic pathways and increased the Li^+ diffusion in the lattice. Similarly, the relative high surface area of the nanotube structure could provide more active surface sites and facilitate fast lithium ion transfer between electrode and electrolyte, thus increasing charge transfer as depicted in EIS results. Moreover, the increase in tubular size to 12 μm as compared to conventional small sized tubes helped in increasing the discharge capacities. Doping of Fe-S, Fe, and S in TNTs increased the interlayer spacing, thus favoring Li^+ intercalation/de-intercalation as well. Fe-S doped TNTs showed best results with exceptional increase in cycling and rate cycling discharge capacities at exceptionally higher rates.

4. Conclusions

Vertically aligned TNTs were successfully prepared via anodization method in a lactic acid added electrolyte. This additive stabilized the TNTs formation and allow to apply the high working voltage of 120 V and also at the high temperature of 60 °C. Co-doping of Fe and S proved to be fruitful as they enhanced electrochemical properties to their maximum as compared to bare TNTs. Increase in Li^+ diffusion (D) and decrease in charge transfer resistance (R_{ct}) resulted in high rate cycling and cycling capabilities. Fe-S doped TNTs achieved a high charge retention and also showed high discharge capacities when compared with bare TNTs. Anodic TiO_2 nanotubular layer is a binder free electrode that especially combined with a doping process shows a high LIB performance and exceptional stabilities.

Declaration of Competing Interest: There are no conflicts to declare

Acknowledgements: This work was supported by the Primary Research Program (21A01042) of the Korea Electro- Technology Research Institute and by the Technology Innovation Program (21A02076) of the Ministry of Trade, Industry & Energy (MOTIE, Korea).

Supplementary materials: Supporting material associated with this article can be found in the online version (doi: Not yet received)

References

[1] Goriparti ,S.; Miele, E.; De Angelis ,F.; Di Fabrizio ,E.; Proietti Zaccaria ,R.; Capiglia ,C. Review on recent progress of nanostructured anode materials for Li-ion batteries. J. Power Sources (2014), 257, 421–443.

[2] Hwang , H.; Kim ,H.; Cho.J. MoS_2 Nanoplates Consisting of Disordered Graphene-like Layers for High Rate Lithium Battery Anode Materials. Nano Lett. (2011), 11, 4826–4830.

[3] Moretti, A.; Kim, G.T.; Bresser, D.; Renger, K.; Paillard, E.; Marassi, R.; Winter, M.; Passerini, S. Investigation of different binding agents for nanocrystalline anatase TiO_2 anodes and its application in a novel, green lithium-ion battery. J. Power Sources (2013), 221, 419–426.
[4] Chen, Z.; Belharouak, I.; Sun, Y.K.; Amine, K. Titanium-Based Anode Materials for Safe Lithium-Ion Batteries. Adv. Funct. Mater. (2013), 23, 959–969.

[5] Wagemaker, M.; Mulder, F.M. Properties and Promises of Nanosized Insertion Materials for Li-Ion Batteries Acc. Chem. Res. (2013), 46, 1206–1215.

[6] Meng, X.; Banis, M. N.; Geng, D.; Li, X.; Zhang, Y.; Li, R.; Abou-Rachid, H.; Sun, X. Controllable atomic layer deposition of one-dimensional nanotubular TiO_2. Appl. Surf. Sci. (2013), 266, 132–140.

[7] Acevedo-Peña, P.; Haro, M.; Rincón, M. E.; Bisquert, J.; Garcia-Belmonte, G. Facile kinetics of Li-ion intake causes superior rate capability in multiwalled carbon nanotube @TiO2nanocomposite battery anodes. J. Power Sources (2014), 268, 397–403.

[8] Guo, Y. G.; Hu, Y. S.; Sigle, W.; Maier. J. Superior Electrode Performance of Nanostructured MesoporousTiO2 (Anatase) through Efficient Hierarchical Mixed Conducting Networks . Adv. Mater. (2007), 19, 2087–2091.

[9] Yang, Y.; Ji, X.; Jing, M.; Hou, H.; Zhu, Y.; Fang, L.; Yang, X.; Chen, Q.; Banks, C. E. Carbon dots supported upon N-doped TiO2 nanorods applied into sodium and lithium ion batteries. J. Mater. Chem. A (2015), 3, 5648–5655.

[10] Lee, K.; Mazare, A.; Schmuki. P.One-Dimensional Titanium Dioxide Nanomaterials: Nanotubes. Chem. Rev. (2014), 114, 9385–9454.

[11] Xu, J.; Wang, Y.; Li, Z.; Zhang,W. F. Preparation and electrochemical properties of carbon-doped TiO_2 nanotubes as an anode material for lithium-ion batteries. J. Power Sources (2008), 175, 903–908.

[12] Andriamiadamanana, C.; Laberty-Robert, C.; Sougrati, M. T.; Casale, S.; Davoisne, C.; Patra, S.; Sauvage, F. Room-Temperature Synthesis of Iron-Doped Anatase TiO2 for Lithium-Ion Batteries and Photocatalysis. Inorganic chem.(2014), 53, 10129-10139.

[13] Lübke, M.; Johnson, I.; Makwana, N. M.; Brett, D.; Shearing, P.; Liu, Z.; Darr, J. A. High power TiO_2 and high capacity Sn-doped TiO2nanomaterialanodes for lithium-ion batteries. J. Power Sources (2015**)**, 294, 94–102.

[14] Zhang, Y.; Du, F.; Yan, X.; Jin, Y.; Zhu, K.; Wang, X.; Li, H.; Chen, G.; Wang, C.; Wei,Y. Improvements in the Electrochemical Kinetic Properties and Rate Capability of Anatase Titanium Dioxide Nanoparticles by Nitrogen Doping. ACS Appl. Mater. Interfaces (2014**)**, 6, 4458–4465.

[15] Lübke, M.; Shin, J.; Marchand, D. Brett, P. Shearing, Z. Liu, J. A. Darr., Highly pseudocapacitive Nb-doped TiO2 high power anodes for lithium-ion batteries. J. Mater. Chem. A (2015**)**, 3, 22908–22914.

[16] Tan, Y. N .; Wong, C. L .; Mohamed, A. R . An Overview on the Photocatalytic Activity of Nano-Doped-TiO2 in the Degradation of Organic Pollutants ISRN Mater. Sci. **(**2011), 2011, 1–18.

[17] Yu, L.; Wang, Z.; Zhang, L.; Wu, H.; Bin , X.; Lou, W. TiO2 nanotube arrays grafted with Fe2O3 hollow nanorods as integrated electrodes for lithium-ion batteries. J. Mater. Chem. A (2013), 1, 122–127.

[18] Chamanzadeh, Z.; Noormohammadi, M. Self-organized and uniform TiO2 nanotube arrays with optimized NH4F concentration in electrolyte by high voltage electrochemical anodization Mater. Res. Express 5 (2018) 055025.

[19] Fang, J.; Liu, W.; Yu, F.; Qin, F.; Wang, M.; Zhang, K.; Lai, Y. Fe, S co-doped anatase TiO2 nanotubes as anodes with improved electrochemical performance for lithium ion batteries. RSC Adv. (2016), 6, 70133–70140.

[20] Macak , J. M.; Tsuchiya, H.; Ghicov, A.; Yasuda, K.; Hahn, R.; Bauer, S.; Schmuki, P. TiO2 nanotubes: Self-organized electrochemical formation, properties and applications. Curr. Opin. Solid State Mater. Sci. (2007), 11, 3–18

[21] Macák, J. M.; Tsuchiya, H.; Schmuki, P. High-Aspect-Ratio TiO2 Nanotubes by

Anodization of Titanium. Angew. Chemie - Int. Ed. (2005), 44, 2100–2102.

[22] Roy, P.; Berger, S.; Schmuki. P. TiO2 Nanotubes: Synthesis and Applications. Angew. Chemie - Int. Ed. (2011), 50, 2904–2939.

[23] Macak, J. M.; Tsuchiya, H.; Taveira, L.; Aldabergerova, S.; Schmuki, P. Smooth Anodic TiO2 Nanotubes. Angew. Chemie - Int. Ed. (2005), 44, 7463–7465.

[24] So, S.; Lee, K.; Schmuki. P. Ultrafast Growth of Highly Ordered Anodic TiO2 Nanotubes in Lactic Acid Electrolytes. J. Am. Chem. Soc. (2012), 134, 11316–11318.

[25] Kowalski, D.; Kim, D.; Schmuki. P. TiO2nanotubes, nanochannels and mesosponge: Self-organized formation and applications. Nano Today (2013), 8, 235–264.

[26] Bayati, M. R.; Moshfegh, A. Z.; Golestani-Fard. F. Micro-arc oxidized S-TiO2nanoporous layers: Cationic or anionic doping?. Mater. Lett. (2010), 64, 2215–2218.

[27] Yan, D.; Yu, C.; Bai, Y.; Zhang, W.; Chen, T.; Hu, B.; Sun, Z.; Pan, L. Sn-doped TiO2 nanotubes as superior anode materials for sodium ion batteries. Chem. Commun. (2015), 51, 8261–8264.

[28] Ni, J.; Fu, S.; Wu, C.; Maier, J.; Yu, Y.; Li, L. Self-Supported Nanotube Arrays of Sulfur-Doped TiO_2 Enabling Ultrastable and Robust Sodium Storage. Adv. Mater. (2016), 28, 2259–2265.

[29] Piatkowska, A.; Janus, M.; Szymanski, K.; Mozia. S. C-, N- and S-Doped TiO2 Photocatalysts: A Review. Catalysts(2021), 11,144.

[30] Bayati, M.R.; Moshfegh, A.Z.; Golestani-FArd, F. Micro-arc oxidized S-TiO2nanoporous layers: Cationic or anionic doping?. Mater. Lett. (2010), 64, 2215-2218.

[31] Ohno, T.; Akiyoshi, M.; Umebayashi, T.; Asai, K.; Mitsui, T.; Matsumura. M. Preparation of S-doped TiO2photocatalysts and their photocatalytic activities under visible light. Appl. Catal. A Gen. (2004), 265, 115–121.

[32] Kang, S. H.; Fang, T. H.; Chen, T. H .; Hsiao ,Y. J.; Hong, Z. H.; Chuang, C. H.;Riccobono, L. Size effect on mechanical properties of TiO2 capped nanotubes investigated using in situ transmission electron microscopy. Microsyst. Technol. (2014), 20 (3), 515–520.

[33] Brumbarov, J.; Vivek, J. P.; Leonardi, S.; Valero-Vidal, C.; Portenkirchner, E.; Kunze-Liebhäuser ,J. Oxygen deficient, carbon coated self-organized TiO2 nanotubes as anode material for Li-ion intercalation. J. Mater. Chem. A (2015), 3, 16469–16477.

[34] Wagemaker, M.; Borghols, W. J. H.; Mulder, F. M. Large Impact of Particle Size on Insertion Reactions. A Case for Anatase LixTiO2. J. Am. Chem. Soc. (2007), 129, 4323–4327.

[35] Auer, A.; Portenkirchner, E.; Götsch, T.; Valero-Vidal, C.; Penner, S.; Kunze Liebhäuser. H. Preferentially Oriented TiO2 Nanotubes as Anode Material for Li-ion Batteries: Insight into Li-Ion Storage and Lithiation Kinetics J. ACS Appl. Mater. Interfaces (2017), 9, 36828–36836.

[36] Aljabali , A. A. A.; Barclay, J. E.; Butt, J. N.; Lomonossoff , G. P.; Evans. D. Redox-active ferrocene-modified Cowpea mosaic virus nanoparticles. J. Dalt. Trans. (2010), 39, 7569–7574.

[37] Pervez ,S.; Kim,D .; Doh, C. H.; Farooq.U.; Yaqub.A.; Choi ,J. H.; Lee, Y. J .; Saleem .M. High areal capacity for battery anode using rapidly growing self-ordered TiO2nanotubes with a high aspect ratio Mater. Lett. (2014), 137, 347–350.

[38] Arrouvel, C.; Parker, S. C.; Saiful Islam, M. Lithium Insertion and Transport in the TiO2-B Anode Material: A Computational StudyChem. Mater. (2009), 21, 4778–4783.

[39] Lee, C. W .; Pang, Q.; Ha, S.; Cheng, L.; Han, S. D.; Zavadil, K. R.; Gallagher, K. G.; Nazar, L. F.; Balasubramanian. M. Directing the Lithium−Sulfur Reaction Pathway via Sparingly Solvating Electrolytes for High Energy Density Batteries. ACS Cent. Sci. (2017), 3, 605–613.

[40] Zhu, K.; Wang, Q.; Kim, J.; Pesaran, A.; Frank. A. J. Pseudocapacitive Lithium-Ion Storage in Oriented Anatase TiO2 Nanotube Arrays. J. Phys. Chem. C (2012), 116, 11895–11899.

[41] Zhang, S.; Zheng, M.; Lin, Z.; Li, N. ; Liu, Y.; Zhao, B.; Pang, H.; Cao, J.; He, P.; Shi, Y.; Activated carbon with ultrahigh specific surface area synthesized from natural plant material for lithium–sulfur batteries. J. Mater. Chem. A (2014), 2, 15889–15896.

[42] Gauthier, M.; Carney, T. J.; Grimaud , A.; Giordano, L.; Pour, N.; Chang, H. H.; Fenning , D. P.; Lux, S. F.; Paschos, O.; Bauer, C.; Maglia, F.; Lupart, S.; Lamp, P.; Shao-Horn ,Y .The Electrode-Electrolyte Interface in Li-ion Batteries: Current Understanding and New Insights. J. Phys. Chem. Lett. (2015), 6, 4653–4672.

[43] Guan, D.; Wang, Y. Electrodeposition of Ag nanoparticles onto bamboo-type TiO2 nanotube arrays to improve their lithium-ion intercalation performance Ionics (2013), 19, 879–885.